Supplementary Information

Scalable Nanoporous Superhydrophobic Films Toward Extreme Icing Conditions at −141°C and Icing Wind Tunnel

Yunyun Meng, [a] Zhengang Pu, [a] Yang Qi, [a] Yanxin Zhang, [b] Suli Xing, [*a] Xian Yi, [*b] Song Wang, [a] Senyun Liu [b] and Nan Wu[*a]

Supplementary Movie Captions

Movie S1. Water droplet impact on the surface of PF10 at ~−12°C.

Movie S2. Water droplet impact on the surface of NS10 at ~−9°C.

Movie S3. Optical and infrared videos of surface condensation on PF10, followed by water jet impact testing to investigate the surface wettability.

Movie S4. Water droplet impact on the surface of PF20 at ~−128°C.

Movie S5. Water droplet impact on the surface of PF20 at ~−141°C.

Movie S6. Water droplet impact on the surface of NS40 at ~−125°C.

Movie S7. Water droplet impact on the surface of PF10 at ~−122°C.

Movie S8. Dynamic melting process of frost layers on the surface of PF10.

Movie S9. Dynamic melting process of frost layers on the surface of NS20.

Movie S10. Icing wind tunnel testing of PF10-PF10 airfoil sample at 0.4 W/cm^2.

Movie S11. Icing wind tunnel testing of PF10-NS20 airfoil sample at 0.4 W/cm^2.

Supplementary Table

Table S1. Comparison of the composition of superhydrophobic coatings reported in literature.

Adhesive	Nanoparticles	c_{NPs} (wt%)	Substrate features	Reference
SiP	F-MOFs@ATP	87.5	Micro/nano porous structures	[1]
PDMS	SiO_2 NPs, TiN	82	Nanoporous structures	[2]
POA	FluoroPOS@silica	71	Convex structures	[3]
PDMS	Montmorillonite	68	Convex structures	[4]
EAA	SiO_2 NPs	61	Nanoporous structures	[5]
Polystyrene	SiO_2 NPs, polypropylene	60	Porous structures	[6]
Epoxy resin	PTFE, carbon powder	55	Micro/nano porous structures	[7]
Epoxy resin	PTFE	30	Nanoporous structures	[8]
PDMS, E51	SiO_2 NPs	29	Hole structures	[9]

Note: SiP is silane modified polyester resin; F-MOFs@ATP is fluorinated MOF modified attapulgite nanoparticles; PDMS is polydimethylsiloxane; SiO_2 NPs are silica nanoparticles; POA is polyolefin adhesive; FluoroPOS@silica is fluorosilane modified silica nanoparticles; EAA is polyethylene acrylic acid.

Table S2. Dynamic anti-icing properties of superhydrophobic surfaces fabricated by different methods

Reference	Substrate temperature (°C)	Structural characteristics	Experiment condition					Fabrication method	Constituent
			Relative humidity	Droplet temperature (°C)	Impacting velocity (*We*)	Surface inclination angle	Drop volume		
Ref.[10]	−5, −10, {−15}*	Single structures	20±5%	Room temperature	0.99 m/s	0°	5 μL	Femtosecond laser processing, surface treatments	Ni, 1H, 1H, 2H, 2H-perfluorodecyltriethoxysilane
Ref.[11]	−5, −10	Random hierarchical structure	/	Room temperature	1 m/s	0°	4 μL	Spraying	Fluorinated SiO_2, PDMS
Ref.[12]	−25	Hierarchical structures	40 ± 5%	Room temperature	1.98 m/s, 4.95 m/s	0°	5 μL	Hydrothermal, spraying	Cerium dioxide, polyurethane
Ref.[13]	−20	Single-textures	2%	Room temperature	2.2 m/s	0°	4 μL	Laser processing, vapor deposition	Silicon
Ref.[14]	−10.7, −17, {−19.7}	Hierarchical structures	<10%	15	0.99 m/s	0°	14 μL	Laser-processing, surface treatments	Aluminum, $C_{13}H_{13}F_{17}O_3Si$
Ref.[15]	−10	Hierarchical structures	<20%	15-20	0.99 m/s	0°	14 μL	Laser-processing, surface treatments	Aluminum, $C_{13}H_{13}F_{17}O_3Si$
Ref.[16]	−30	Hierarchical structures	60%	26.4	2.43 m/s	0°	11.5 μL	FC3150 coating	Fluorocarbon resin, clay, fumed silica, Low surface energy reagent
Ref.[17]	−5, {−30}	Hierarchical structures	10±5%	−5	3.6 m/s	0°	4.2 μL	photolithography technology and plasma etching,	Silicon,
Ref.[17]	−5, {−20}	Nanostructures	10±5%	−5	3.6 m/s	0°	4.2 μL	spraying	commercial Glaco agent
Ref.[18]	−10	Hierarchical structures	50±5%	5	0.77 m/s	3°	4.2 μL	Stöber method	Graphene oxide, SiO_2
Ref.[19]	−20, {−24}, {−35}	Hierarchical structures	15±2%	Room temperature	(28.21)△	0°	/	Spraying	Commercial Neverwet agent

Ref.[20]	−25, {−30}	Post-array surface	7%	−5 ± 0.5	(20.4)	0°	/	Wire-cutting machining, corrosion, surface treatments	Cu
Ref.[21]	−20, {−30}	Hierarchical structures	<5%	Room temperature	(28)	0°	4 μL	Sand blasting, hydrothermal treatment, surface modification	Ti6Al4V sheets
Ref.[22]	−15	Hierarchical structures	<2%	22	2.2 m/s (138)	0°	/	/	/
Ref.[23]	−25	Hierarchical structures	10%	−5	3.4 m/s	0°	4.2 μL	Laser-processing	Al specimens
Ref.[7]	{−8}	Hierarchical structures	/	20	0.6 m/s	25°	13 μL	Spraying	Epoxy resin, carbon, PTFE
NS10	{−9}, {−10}	Hierarchical structures							
NS20	{−116}	Hierarchical structures							
NS40	{−120}	Hierarchical structures	55±3%	20	1.4 m/s (91.6)	5°	50 μL	Spraying	Fluorinated epoxy resin, SiO_2, MWCNT
PF10	−10, −12, −122	Nanoporous structures							
PF20	−128, −141	Nanoporous structures							

* Droplets adhere after impacting the surface at this temperature (in braces).

△ The value in parenthesis is the Weber (*We*) number of impacting water.

Table S3. Comparison of the anti-icing investigation through icing wind tunnel between this work and previous reports.

Structured method	Structural characteristics	Contact angle (°)	Experiment condition					Without heating	Electric heating		Ref.
			WS (m/s)	LWC (g/m^3)	MVD (μm)	TOA (°C)	T_s (s)		P_{anti}	*ESP*	
Ultrafast laser ablation	Hierarchical structures	156.8±2	30	3	30.48	29		Pinning			[24]
Spraying		155.68	10			−10	120	Icing			[25]
Anodization	Spongy micro-structure	158	10		67	−10		Icing			[26]
Spraying	Porous polysynaptic coral-like structures	159.5	50	2	35	−10	300	Icing			[27]
Spraying	Porous micro-nano structures	154.49	6			−6	300	Icing			[28]
Laser processing	Dual-scale hierarchical structures	165.6	50	1	20	−5	30	Icing			[23]
Etching process	Periodic single-stage structure	152.5±1	25±1	0.644±0.05	18.3	−10±0.5			13.8 W	30.3%	[29]
Bonding	Superhydrophobic film	152.5	10.5	0.5	20	−10	60	Icing	58 W	38.57%	[30]
Spraying	rough ‘honeycomb structure	160	42	2	30	−5.5	20	Icing	0.98 W/cm^2	59.5%	[31]
Spraying	Micro-nano porous structure	162.3	10			−5	120	Icing	2 W/cm^2		[32]
Spraying		157	40	2		−5		Icing	0.78 W/cm^2		[33]

Spraying	Porous micro-nano structures	153.42	40	2	20	−7	15	Icing	0.7 W/cm^2	76.7%	[34]
Laser ablation	Periodic microgrooves	156.02	40	2	20	−7	120	Icing	0.7 W/cm^2	76.7%	[34]
Direct laser interference patterning	Hierarchical pillar-like structures	163±6	65	0.2	20	−10	300	Icing	0.5 W/cm^2	~60%	[35]
Spraying	**Nanoporous structures**	**153±2.5**	**20**	**2.82**	**20**	**−6±0.5**	**300**	**Icing**	**0.4 W/cm^2**	**33%**	**This work**

Notes: WS, wind speed; LWC, liquid water content; MVD, medium volumetric diameter; TOA, temperature of airflow, T_s, test time; P_{anti}, anti-icing power density of the testing group; *ESP*, energy saving percentage of the test group relative to the control group

Supplementary Note S1. Nanoparticle content of sprayed coatings

Spray-coating technology has garnered significant research interest for fabricating superhydrophobic surfaces, owing to its cost-effectiveness, substrate versatility, and scalability. To contextualize our work, we summarized the slurry compositions of state-of-the-art sprayable superhydrophobic coatings in Table S1. Notably, from the perspective of structural characteristics, superhydrophobic structures can be divided into pore structure, convex structure and porous structure[36, 37]. The hole structure often shows high contact angle lag, which is not conducive to anti-wetting and anti-icing performances. Thus, the surface morphology formed by spraying is usually composed of porous structure and convex structure. The nanoparticle content c_{NPs} in the coating is calculated as:

$$c_{\mathrm{NPs}} = m_{\mathrm{NPs}} / \left(m_{\mathrm{NPs}} + m_{\mathrm{adhesive}} + m_{\mathrm{curing}} \right)$$

where m_{NPs}, m_{adhesive}, and m_{curing} represent the mass of nanoparticles, binder, and curing agent, respectively. Our analysis reveals that achieving superhydrophobicity typically requires a high nanoparticle content, often exceeding 30 wt%[1-9]. Additionally, these approaches frequently necessitate additional steps, such as molecular modification of resins with low-surface-energy groups and intricate structural design of nanoparticles (e.g., fluorinated MOFs-modified attapulgite (F-MOFs@ATP), fluoroalkylsilane-modified silica (FluoroPOS@silica)). This overview underscores a prevalent trade-off: high nanoparticle loadings are common for functionality, often at the expense of simplified processing or robust interfacial adhesion. Our strategy addresses this by enabling robust, nanoporous superhydrophobic structures with substantially lower nanoparticle content and higher resin proportion.

Supplementary Note S2. The regulation of nanoporous structures to water vapor and liquid water

The phase transition of water vapor to condensate droplets can be effectively inhibited by nanoporous structures. As the saturated water vapor pressure decreases

with temperature reduction, supersaturated water vapor generated in low-temperature conditions tends to condense within microstructures[38-41]. Nanoporous structures can inhibit this transition by regulating the vapor pressure. For a hydrophobic nanocavity ($\cos\theta<0$), the Kelvin equation dictates that the vapor pressure inside the cavity (P_r) is higher than the ambient saturation pressure (P_{sat}). This elevated vapor pressure helps stabilize the vapor phase and suppress condensation, offering a quantitative means to evaluate the impact of structural scale on anti-wetting performance. As shown in Fig. 1b, the internal equilibrium vapor pressure decreases sharply as the pore size increases, eventually converging with the external ambient pressure. For instance, when T=273.15 K, P_{sat}=608.2 Pa, σ_{lg}=0.07564 N/m, θ=110°, V_l=18.028 cm^3/mol, R=8.314 J·mol^{-1}·K^{-1}, P_r can be calculated as approximately 660.3 Pa at a=10 nm, while it drops to about 613.2 Pa at a=100 nm, approaching the external reference value.

Even for condensed liquid water, nanoporous surfaces still exhibit excellent repellency. As shown in Fig. 1c, when a droplet contacts the nanoporous surface in the C-B state, the apparent contact angle decreases with solid-liquid contact fraction (f). According to the stereological principle (Delesse's principle), the solid-liquid contact fraction can be approximated as porosity due to the homogeneity and isotropy of nanoporous structures. In fact, the porosity of the porous structures formed by fine nanoparticles (4-40 nm in diameter) can reach more than 90% (f<10%). At such a low contact fraction, hydrophobic substrates with intrinsic contact angle between 90° to 120° can easily achieve apparent contact angles exceeding 150° (Fig. 1b). Notably, the common low surface energy modification can yield the intrinsic contact angle ranging from 100° to 120°[42, 43]. When $\theta_Y = 100°$, the apparent contact angle can reach 156.5° for a relatively small solid-liquid contact fraction (f<10%).

Supplementary Note S3. Bouncing condition of impacting water

We analyze the dynamic impact of water droplets on ultra-low temperature surfaces by considering three key energetic parameters: adhesion energy (E_{w}), surface energy (ΔE_{sur}), and energy dissipation (ΔE_{vis}). As shown in Fig. S10, the impacting droplet experiences three stages, i.e. penetration, retraction, and detachment, and are denoted by 1, 2, and 3 in the subscript. During the impacting and penetration stage, the droplet deforms from sphere to pancake shape, accompanied by initial impacting kinetic energy (E_{k}) transforming to viscous dissipation, surface energy, and adhesion work:

$$\Delta E_1 = E_{\mathrm{k}} - (\Delta E_{\text{vis-vol1}} + \Delta E_{\text{vis-int1}} + \Delta E_{\text{sur1}} + \Delta E_{\text{w1}})$$

where $\Delta E_{\text{vis-vol1}}$ and $\Delta E_{\text{vis-int1}}$ are the volume part and surface part of energy dissipation caused by viscous friction, respectively. During the retraction stage, the pancake recovers to a sphere droplet with a similar energy transfer:

$$\Delta E_2 = \Delta E_1 - (\Delta E_{\text{vis-vol2}} + \Delta E_{\text{vis-int2}} + \Delta E_{\text{sur2}} + \Delta E_{\text{w2}})$$

In the detachment stage, the residue kinetic energy ($E_{\mathrm{k}}^{'}$) should be expressed by:

$$E_{\mathrm{k}}^{'} = \Delta E_2 - \Delta E_{\text{w3}}$$

Therefore, the actual bouncing condition should be defined as:

$$E_{\mathrm{k}}^{'} = E_{\mathrm{k}} - (\Delta E_{\text{vis-vol1}} + \Delta E_{\text{vis-int1}} + \Delta E_{\text{sur1}} + \Delta E_{\text{w1}}) - (\Delta E_{\text{vis-vol2}} + \Delta E_{\text{vis-int2}} + \Delta E_{\text{sur2}} + \Delta E_{\text{w2}}) - \Delta E_{\text{w3}} > 0$$

Notably, $\Delta E_{\text{sur1}} + \Delta E_{\text{sur2}} = 0$ can be derived according to the evolution of the droplet shape in the penetration and retraction stages. Therefore, the bouncing condition should be:

$$E_{\mathrm{k}}^{'} = E_{\mathrm{k}} - (\Delta E_{\text{vis-vol1}} + \Delta E_{\text{vis-int1}} + \Delta E_{\text{vis-vol2}} + \Delta E_{\text{vis-int2}}) - (\Delta E_{\mathrm{w1}} + \Delta E_{\mathrm{w2}} + \Delta E_{\mathrm{w3}})$$
$$= E_{\mathrm{k}} - (\Delta E_{\text{vis-vol}} + \Delta E_{\text{vis-int}}) - (\Delta E_{\mathrm{w(1+2)}} + \Delta E_{\mathrm{w3}}) > 0$$

Supplementary Note S4. Design of dynamic anti-icing superhydrophobic surface

To diminish energy dissipation and adhesion work, the related structural/chemistry parameters of superhydrophobic surfaces are investigated. The adhesion work includes two aspects. The work needed to overcome contact angle hysteresis in the penetration and retraction stages can be expressed as[44]:

$$E_{\mathrm{w(1+2)}} = (\Delta E_{\mathrm{w1}} + \Delta E_{\mathrm{w2}}) \propto \left(\cos\theta_{\mathrm{rec}} - \cos\theta_{\mathrm{adv}}\right) / \left(1 - \cos\theta_{\mathrm{Y}}\right)$$

where θ_{rec}, θ_{adv}, and θ_{Y} are recoding angle, advancing angle, and Young angle, respectively. Additionally, at the detachment stage, ΔE_{w3} can be determined by:

$$\Delta E_{\mathrm{w3}} = \gamma_{\mathrm{L}} \mathrm{A}_{\mathrm{con}} (1 + \cos\theta_{\mathrm{Y}})$$

where γ_{L} and $\mathrm{A}_{\mathrm{con}}$ are surface tension of water and apparent contact area between droplet and sample surface. Therefore, smaller contact angle hysteresis and larger Young contact angle can yield smaller adhesion work.

The other factor affecting the behaviors of impacting water is energy dissipation. In fact, the volume part and surface part of energy dissipation are both proportional to water viscosity[45], which is inversely related to temperature[46]. Therefore, in low-temperature icing environments, the reduction of water temperature should be suppressed. According to the Fourier heat conduction formula, the involving heat transfer between impacting water and superhydrophobic surface can be expressed as:

$$\Phi = \left(T_{\mathrm{w}} - T_{\mathrm{s}}\right) / R$$

where Φ is the heat transfer between water and superhydrophobic surface, T_{w} and T_{s} are temperatures of water and surface, respectively. R is the thermal resistance from

the droplet to the surface, which can be expressed as[1, 47]:

$$R = \left(h - hX_{\mathrm{i}}\right) / \left(2S_{\mathrm{ws}}\lambda_{\mathrm{s}}\right) + \left(hX_{i}\right) / \left(2S_{\mathrm{ws}}\lambda_{\mathrm{i}}\right)$$

where λ_s and λ_i are the thermal conductivity of the surface and ice, respectively, X_i is the influence factor of the thermal conductivity of ice, h is the heat transfer coefficient between the water droplet and the surface, and S_{ws} is the contact area between the water droplet and the surface. Thus, the thermal conductivity of the structured surface is expected to reduce wherever possible to yield a lower heat transfer.

Supplementary Figures

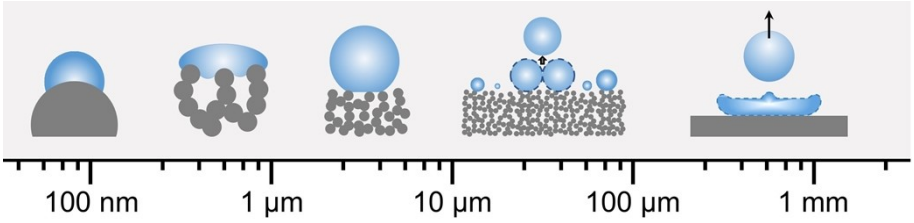

Fig. S1 The cross-size evolution process of liquid water and the anti-wetting mechanisms.

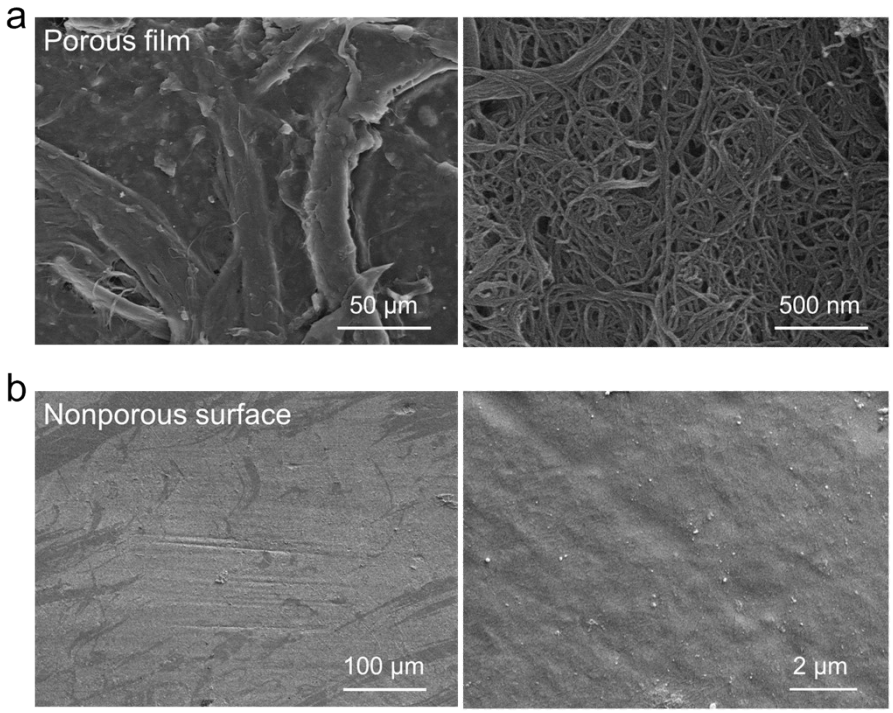

Fig. S2 SEM images of the spraying substrates of (a) porous film and (b) nonporous surface.

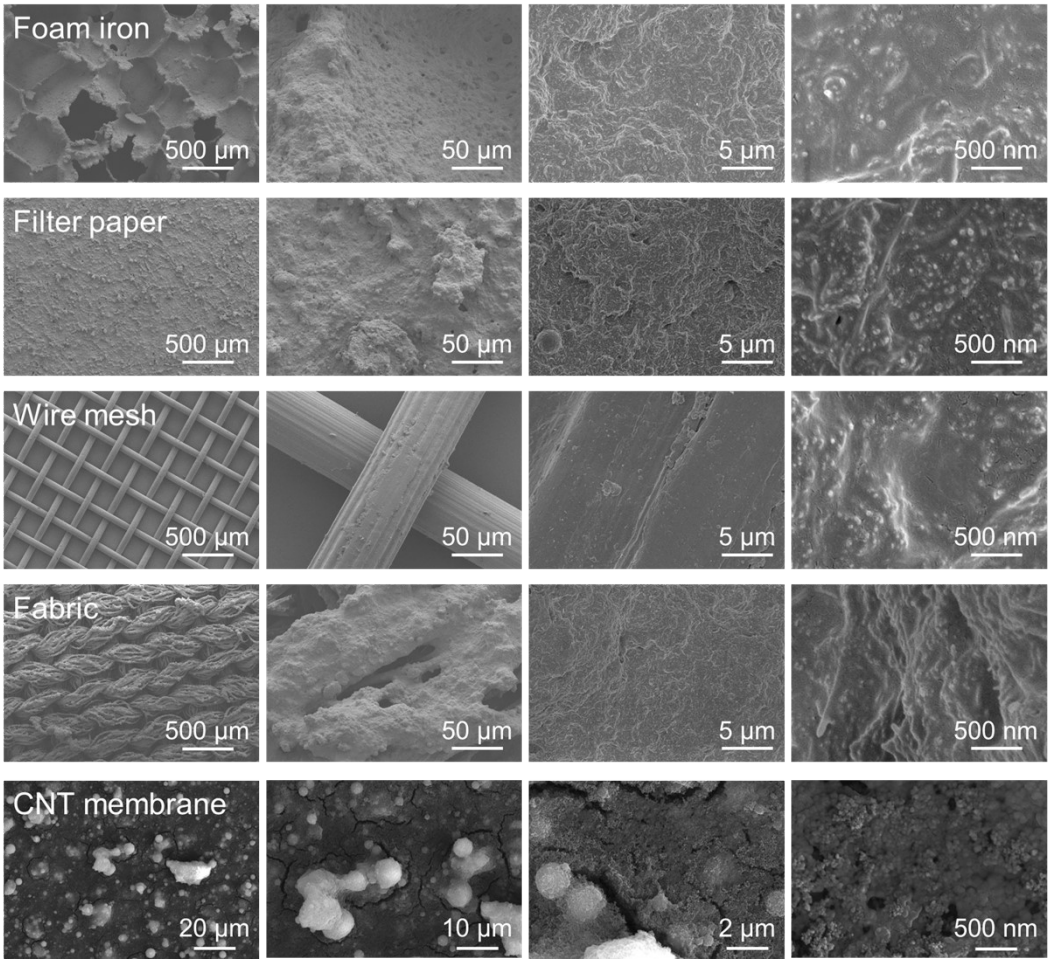

Fig. S3 SEM images of spray coating on different substrates. Although the slurry is completely identical, the morphology obtained by spraying on these porous substrates is completely different from that of FP substrates.

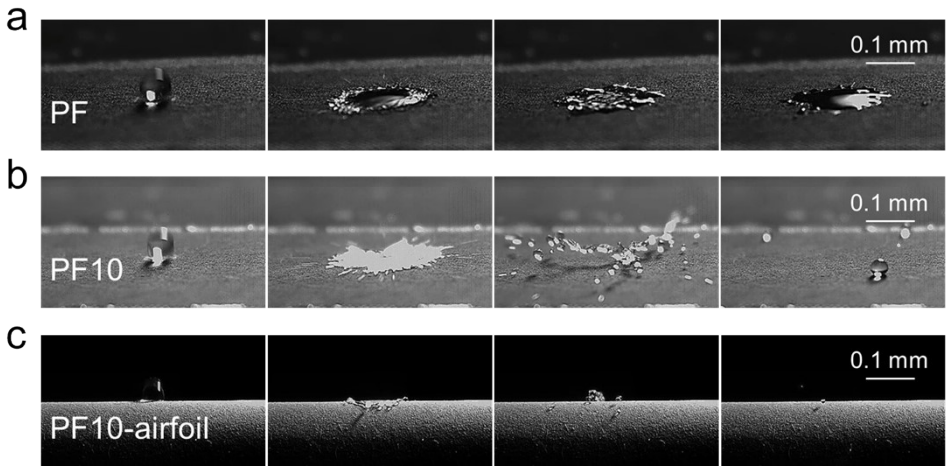

Fig. S4 High-speed snapshots of water impacting the surfaces of (a) PF, (b) PF10, and (c) PF10-airfoil from a height of 10 cm.

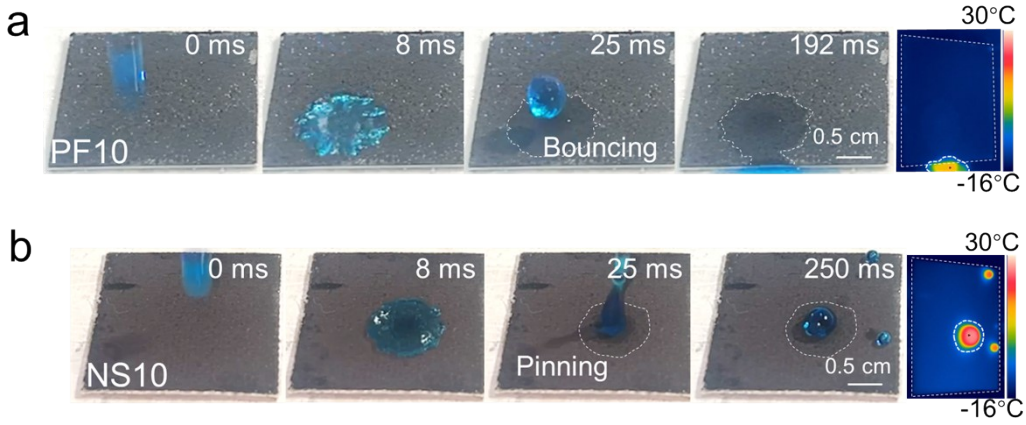

Fig. S5 Top-view optical and corresponding infrared images of droplet impact on (a) PF10 surface at −12°C and (b) NS10 surface at −9°C. Top-down perspective coupled with infrared thermography confirmed the complete rebound of droplets from the PF10 surface at an even lower temperature of −12°C. Conversely, under milder conditions (−9°C), the droplet was pinned on the NS-based surface with only partial rebound.

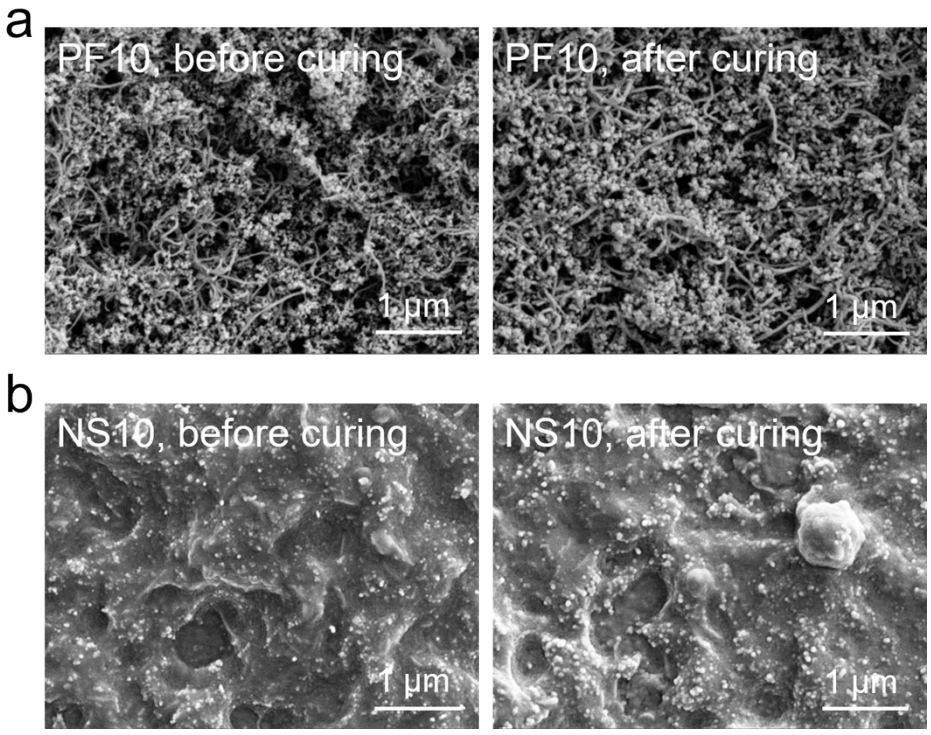

Fig. S6 SEM images of (a) PF10 and (b) NS10 before and after heating curing. No significant changes were observed in the surface microstructure before and after curing, indicating that the thermal curing is not the key factor determining the morphology.

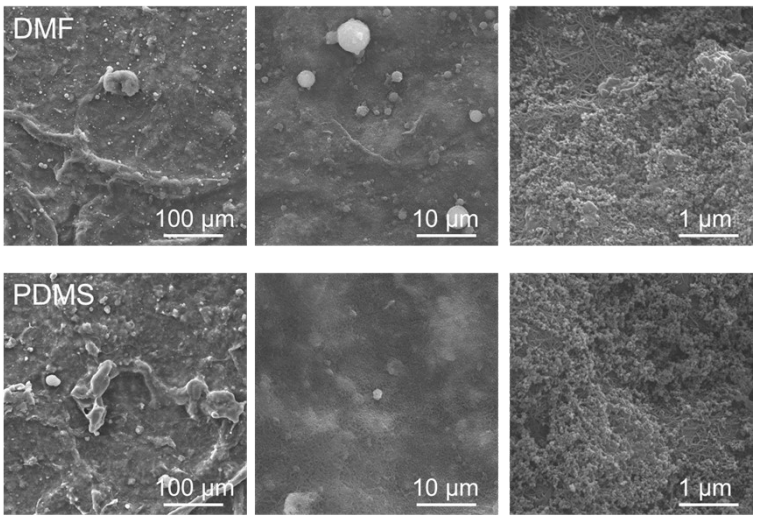

Fig. S7 SEM images of spraying coatings on PF substrate fabricated by replacing the ethyl acetate solvent by N, N-dimethylformamide (DMF), and the fluorinated epoxy resin (F-E51) by polydimethylsiloxane (PDMS). The obtained similar nanoporous structures indicated the independence of resin and solvent in substrate-driven nanoporous structures.

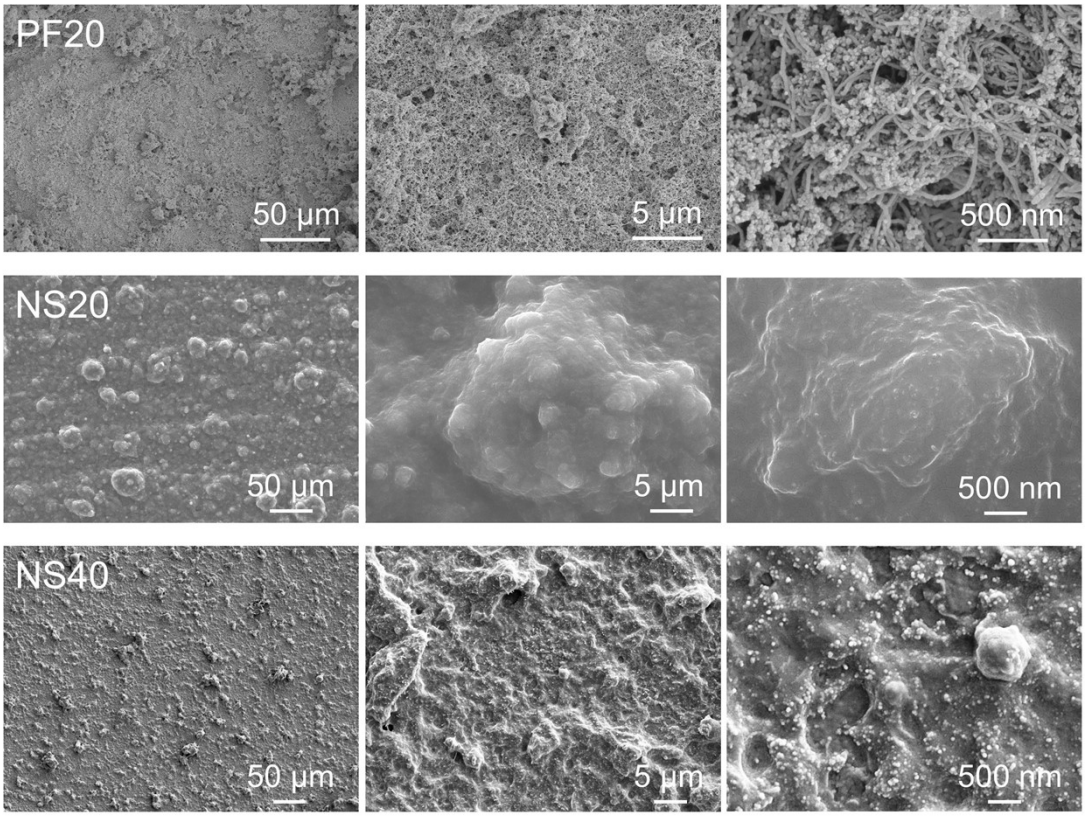

Fig. S8 SEM images of PF20, NS20, and NS40. PF20 exhibited more pores and rougher structures than NS20, demonstrating a similar structural difference to that between PF10 and NS10.

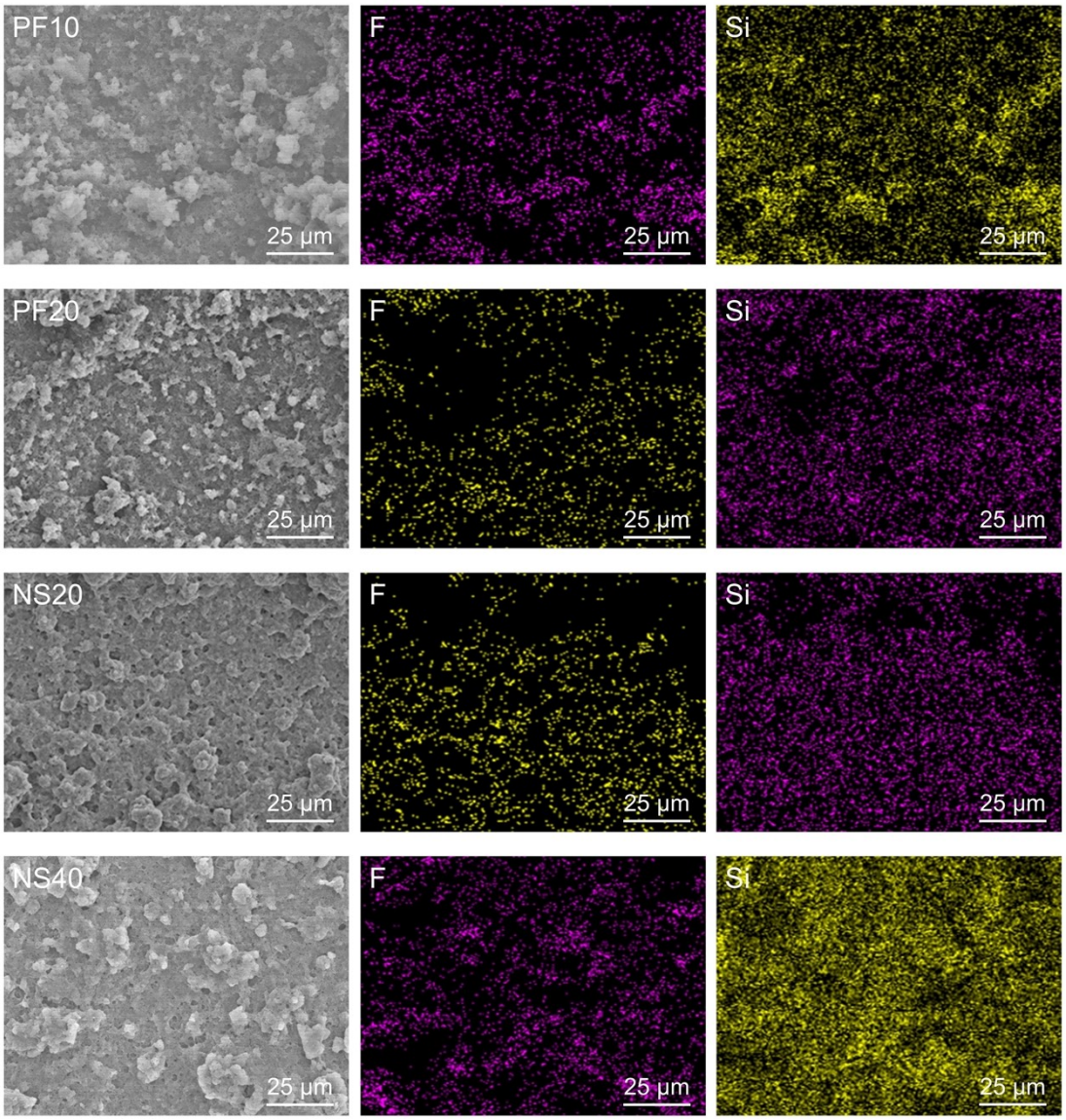

Fig. S9 SEM images and corresponding EDS mappings of Si and F elements of PF10, PF20, NS20, and NS40.

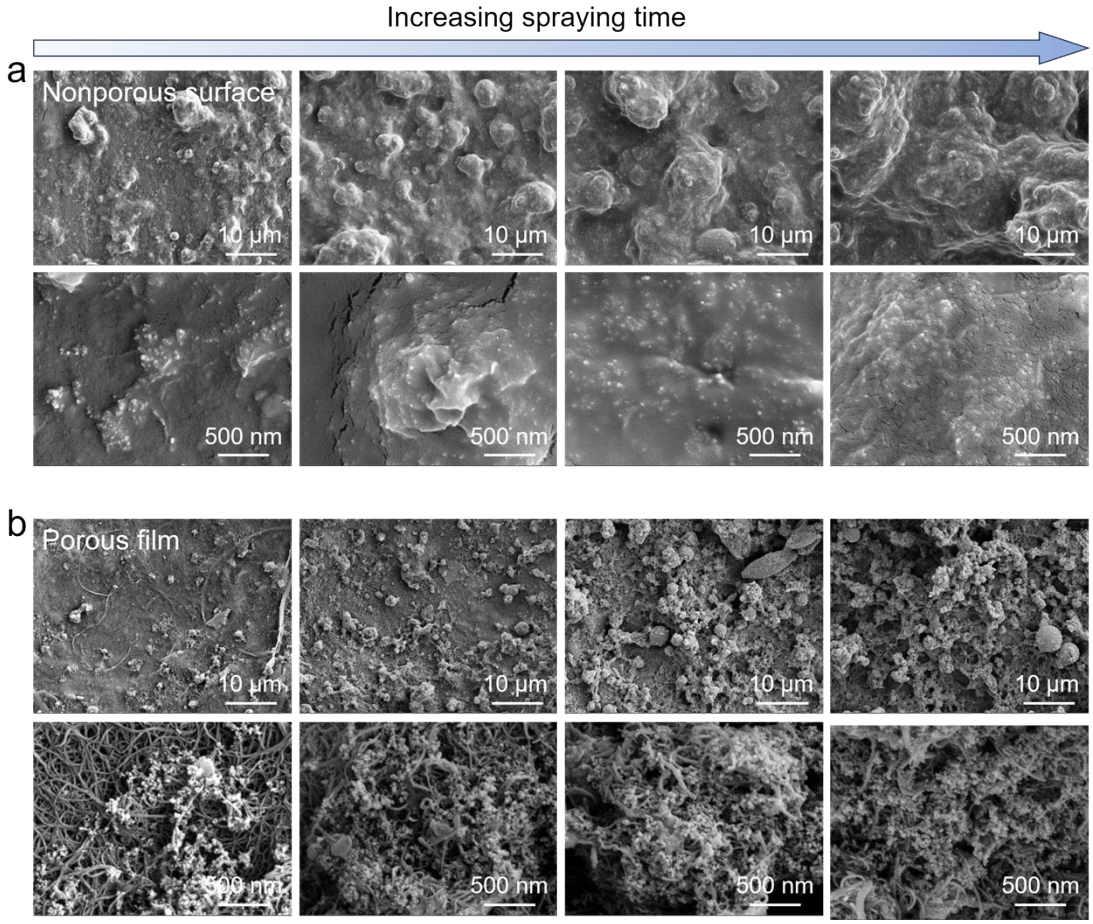

Fig. S10 Evolution of micromorphology with spraying amount on (a) nonporous substrate and (b) porous film.

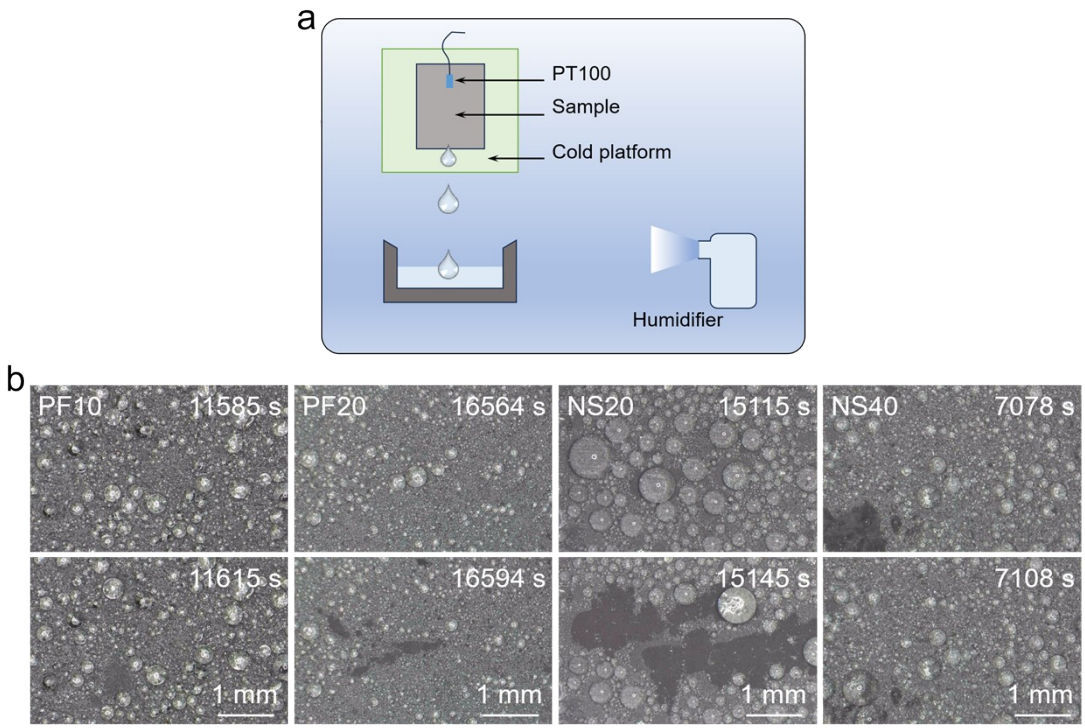

Fig. S11 (a) Schematic diagram of the anti-condensation test. (b) Images showing the condensate droplets detaching from different sample surfaces.

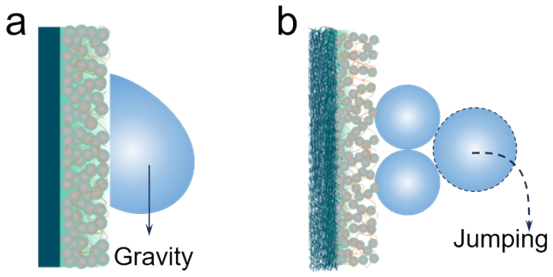

Fig. S12 Schematic diagrams of different detachment modes of condensate droplets: (a) gravity and (b) coalescence-induced jumping

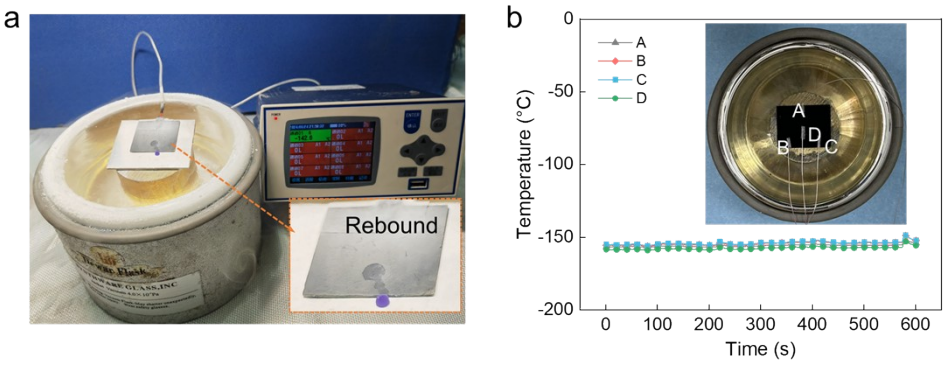

Fig. S13 (a) Optical photograph showing the droplet impacting the sample surface cooled by liquid nitrogen. The surface temperature was monitored in real-time using a PT100 thermometer and recorded by a paperless recorder. The inserted image shows the droplet bouncing off the surface and sliding onto the low-temperature testing platform. (b) The temperature test curves at different positions on the sample surface. The temperature at the center (impact area) is relatively low, but the temperature difference from the other three points is not more than 5 °C.

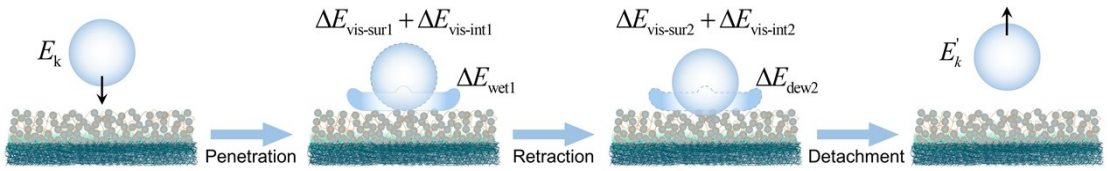

Fig. S14 Schematic diagrams representing penetration, retraction, and detachment stages of droplet impacting on the PF10 surface.

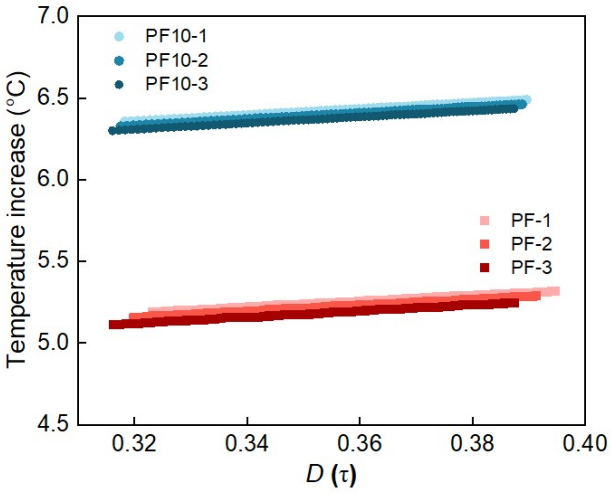

Fig. S15 The thermal conductivity curves of the pristine film (PF) and the nanoporous superhydrophobic film (PF10), each sample was measured three times. The calculated thermal conductivity of the former and the latter were 77.1 ± 1.1 W/K and 58.1 ± 0.4 W/K, respectively.

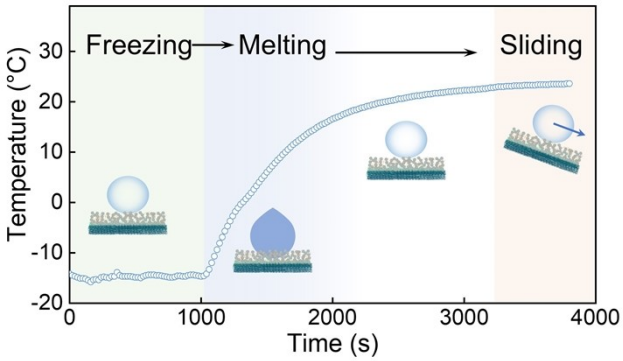

Fig. S16 Temperature curve of the sample surface during the freezing/melting cycle. The insert schematic diagrams represent the changes in droplet morphology. The freezing process is conducted at −15°C while the melting process is implemented with naturally warming environment by turning off the cooling system.

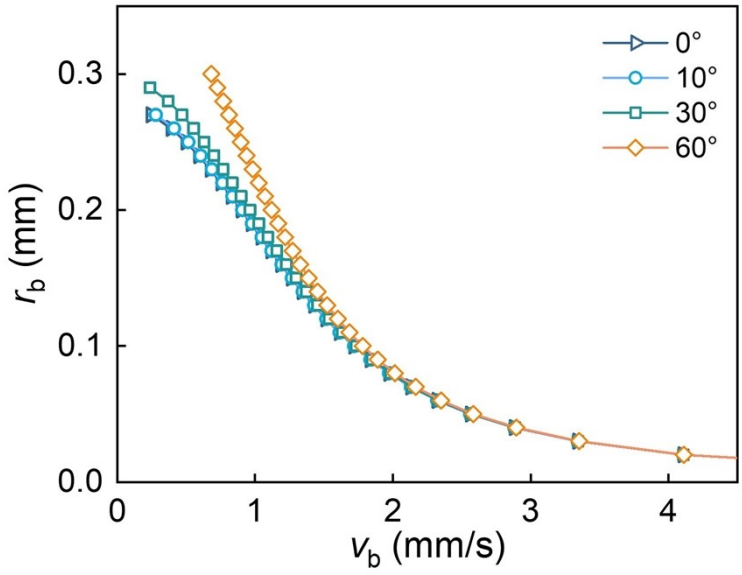

Fig. S17 Critical bubble radius for moving toward interface between ice/water and sample surface changing with moving velocity under different surface inclination angles. When the bubble radius is larger than the critical radius, they will move toward the interface to facilitate superhydrophobic recovery. Therefore, the inclined surface will promote the downward movement of large bubbles, but has little effect on the small bubbles, as the tilt significantly reduces buoyancy, which has a more pronounced effect on large bubbles.

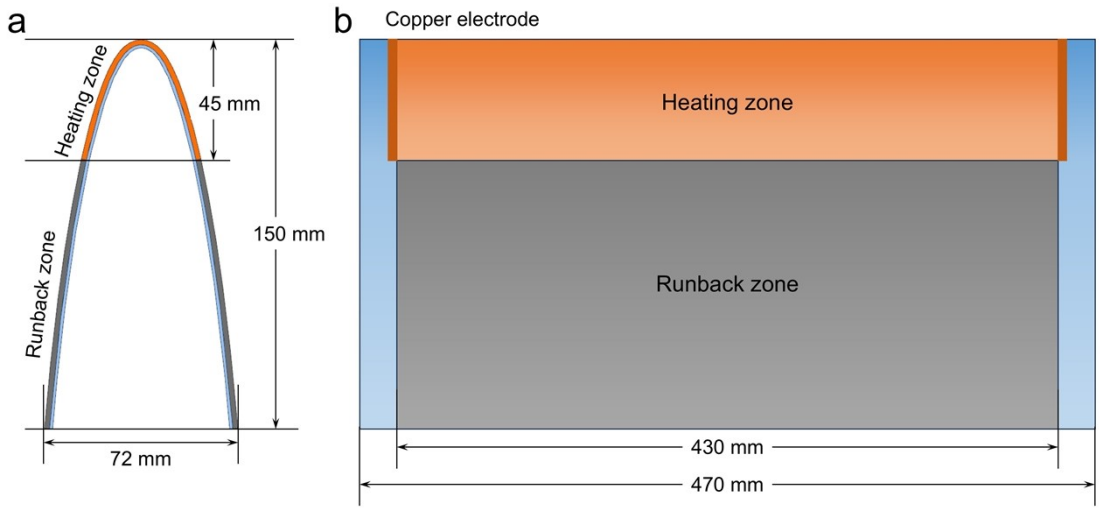

Fig. S18 (a) Sectional view and (b) front view of the composite airfoil for icing wind tunnel test. The heating zone and runback zone are represented by orange and grey, respectively.

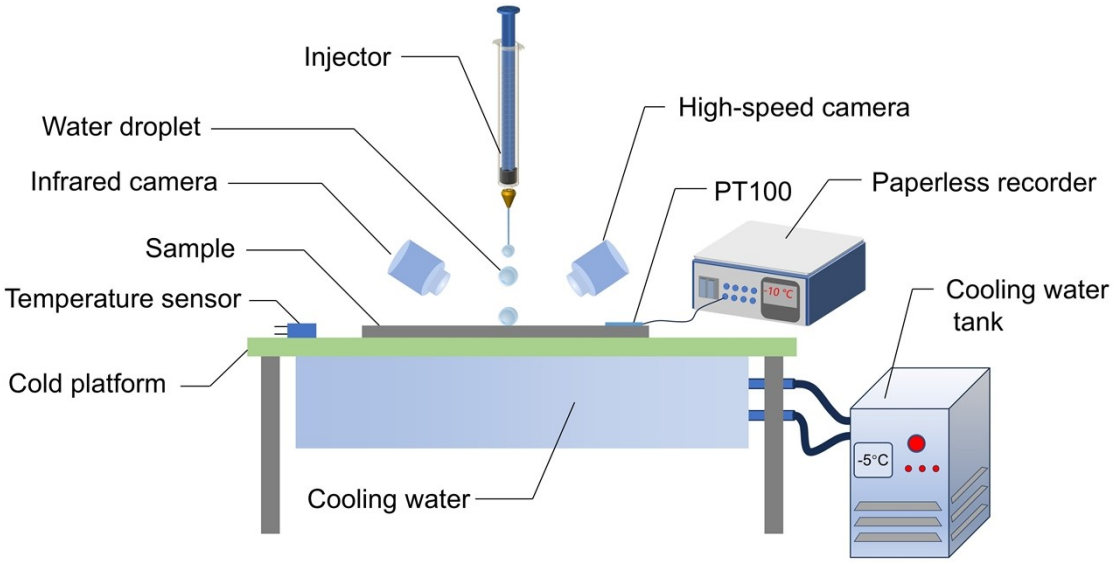

Fig. S19 Schematic diagram of the water-impacting test.

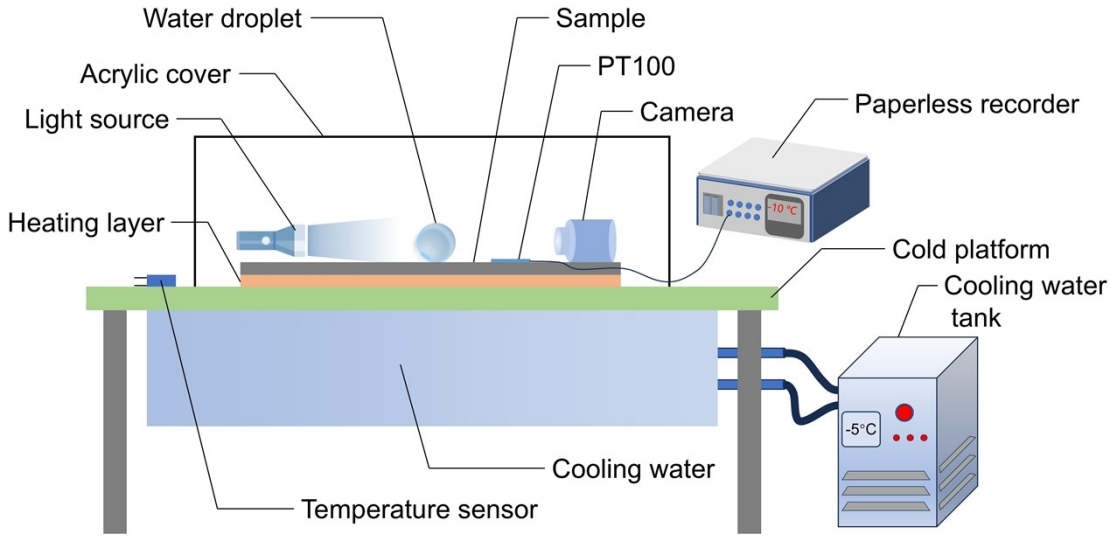

Fig. S20 (a) Schematic diagram and (b) optical photo of the water freezing/melting test.

Reference

1. M. Mao, J. Wei, B. Li, L. Li, X. Huang and J. Zhang, Nat. Commun., 2024, 15, 9610.
2. J. Huang, Z. Peng, B. Zhang, Y. Yao and S. Chen, ACS Appl. Mater. Interfaces, 2024, 16, 44210-44224.
3. J. Wei, J. Zhang, X. Cao, J. Huo, X. Huang and J. Zhang, Nat. Commun., 2023, 14, 2862.
4. Y. Chen, H. Liu, L. Yu, Q. Duan, Z. Ji and L. Chen, ACS Sustainable Chem. Eng., 2020, 8, 10423-10430.
5. H. Luo, M. Yang, D. Li, Q. Wang, W. Zou, J. Xu and N. Zhao, ACS Appl. Mater. Interfaces, 2021, 13, 13813-13821.
6. L. Zhang, X. Xue, H. Zhang, Z. Huang and Z. Zhang, Compos. Part A: Appl. Sci. Manuf., 2021, 146, 106405.
7. Z. Zhao, H. Chen, Y. Zhu, X. Liu, Z. Wang and J. Chen, Compos. Sci. Technol., 2022, 227, 109578.
8. C. Peng, Z. Chen and M. K. Tiwari, Nat. Mater., 2018, 17, 355-360.
9. L. B. Zhang, H. X. Zhang, Z. J. Liu, X. Y. Jiang, S. Agathopoulos, Z. Deng, H. Y. Gao, L. Zhang, H. P. Lu, L. J. Deng and L. J. Yin, J. Colloid Interface Sci., 2022, 630, 1-10.
10. Z. Chen, L. Song, Y. Wang, H. Tao, Z. Liu, T. Wang, F. Ye, Y. He and J. Lin, Appl. Surf. Sci., 2024, 655, 159454.
11. Y. Shen, Y. Wu, J. Tao, C. Zhu, H. Chen, Z. Wu and Y. Xie, ACS Appl. Mater.

Interfaces, 2019, 11, 3590-3598.

12. S. P. Fu, R. P. Sahu, E. Diaz, J. R. Robles, C. Chen, X. Rui, R. F. Klie, A. L. Yarin and J. T. Abiade, Langmuir, 2016, 32, 6148-6162.
13. A. Alizadeh, M. Yamada, R. Li, W. Shang, S. Otta, S. Zhong, L. Ge, A. Dhinojwala, K. R. Conway, V. Bahadur, A. J. Vinciquerra, B. Stephens and M. L. Blohm, Langmuir, 2012, 28, 3180-3186.
14. B. Ding, H. Wang, X. Zhu, R. Chen and Q. Liao, Int. J. Heat Mass Transfer, 2018, 124, 1025-1032.
15. B. Ding, H. Wang, X. Zhu, R. Chen and Q. Liao, Int. J. Heat Mass Transfer, 2019, 138, 844-851.
16. X. Wang, Z. Tang, B. Xu and Z. Chen, Appl. Surf. Sci., 2021, 566, 150717.
17. H. Zhang, X. Zhang, F. He, C. Lv and P. Hao, Int. J. Heat Mass Transfer, 2022, 195, 123196.
18. Z. Chu, W. Jiao, Y. Huang, M. Yan, Y. Zheng, R. Wang and X. He, Adv. Mater. Interfaces, 2020, 7, 2000492.
19. S. Gao, Q. Jia, S. Shi, Z. Liu, B. Wei, Y. Wang, S. Zheng, Y. Yang and X. Wang, Phys. Fluids, 2024, 36, 037133.
20. C. Guo, L. Liu, R. Yang, J. Lu and S. Liu, Langmuir, 2023, 39, 10199-10208.
21. Y. Shen, J. Tao, G. Wang, C. Zhu, H. Chen, M. Jin and Y. Xie, J. Phys. Chem. C, 2018, 122, 7312-7320.
22. A. Alizadeh, V. Bahadur, S. Zhong, W. Shang, R. Li, J. Ruud, M. Yamada, L. Ge, A. Dhinojwala and M. Sohal, Appl. Phys. Lett., 2012, 100, 111601.

23. Z. Tian, L. Wang, D. Zhu, C. Chen, H. Zhao, R. Peng, H. Zhang, P. Fan and M. Zhong, ACS Appl. Mater. Interfaces, 2023, 15, 6013-6024.
24. K. Ma, G. Lin, H. Jin, Q. Jia, H. Sun, X. Bu, X. Shen and D. Wen, Int. J. Heat Mass Transfer, 2023, 209, 124164.
25. Z. Liu, F. Feng, Y. Li, Y. Sun and K. Tagawa, Surf. Coat. Technol., 2023, 457, 129299.
26. L. Foroughi Mobarakeh, R. Jafari and M. Farzaneh, Appl. Surf. Sci., 2013, 284, 459-463.
27. L. Yang, Y. Li, D. Huan, Y. Yang, J. Wang and C. Zhu, J. Mater. Sci., 2023, 58, 16322-16335.
28. Z. Liu, Y. Li, Y. Sun, F. Feng and K. Tagawa, Renewable Energy, 2023, 210, 618-626.
29. S. Xue, Y. Liu, Y. Wang, B. Xiao, X. Shi, J. Yao, X. Lv, W. Yuan, Y. He and M. Tawfik, Int. J. Aerosp. Psychol., 2022, 2022, 1-9.
30. S. Wang, S. Chang, H. Qi and H. Zhao, Appl. Therm. Eng., 2024, 238, 122045.
31. D. Zeng, Y. Li, H. Liu, Y. Yang, L. Peng, C. Zhu and N. Zhao, Colloids and Surfaces A, 2023, 660, 130824.
32. K. Li, Q. Wang, X. Zhou, Y. He, Y. Shi, M. Qin, B. Wu, N. Chen, R. Liu and X. Yi, ACS Appl. Nano Mater., 2024, 7, 24847-24856.
33. L. Gao, Y. Liu, L. Ma and H. Hu, Renewable Energy, 2019, 140, 943-956.
34. H. Sun, G. Lin, H. Jin, X. Bu, C. Cai, Q. Jia, K. Ma and D. Wen, Renewable Energy, 2021, 179, 1179-1190.

35. S. Alamri, V. Vercillo, A. I. Aguilar-Morales, F. Schell, M. Wetterwald, A. F. Lasagni, E. Bonaccurso and T. Kunze, Adv. Mater. Interfaces, 2020, 7, 2001231.
36. Y. Lai, X. Gao, H. Zhuang, J. Huang, C. Lin and L. Jiang, Adv. Mater., 2009, 21, 3799-3803.
37. Y. Shen, J. Tao, Z. Chen, C. Zhu, G. Wang, H. Chen and S. Liu, ACS Sustainable Chem. Eng., 2018, 6, 9958-9965.
38. A. Azimi Yancheshme, G. Momen and R. Jafari Aminabadi, Adv. Colloid Interface Sci., 2020, 279, 102155.
39. R. Wang, F. Wu, D. Xing, F. Yu and X. Gao, ACS Appl. Mater. Interfaces, 2020, 12, 24512-24520.
40. G. Heydari, M. Sedighi Moghaddam, M. Tuominen, M. Fielden, J. Haapanen, J. M. Makela and P. M. Claesson, J. Colloid Interface Sci., 2016, 468, 21-33.
41. A. Khaskhoussi, E. Rahimi, L. Calabrese, A. Cornet, P. R. Anusuyadevi, P. Gonugunta, A. Mol and E. Proverbio, Chem. Eng. J., 2025, 515, 163767.
42. E. Burkarter, C. K. Saul, F. Thomazi, N. C. Cruz, L. S. Roman and W. H. Schreiner, Surf. Coat. Technol., 2007, 202, 194-198.
43. V. Sharma, V. Sharma, M. S. Goyat, A. Hooda, J. K. Pandey, A. Kumar, R. Gupta, A. K. Upadhyay, R. Prakash, J. B. Kirabira, P. Mandal and P. K. Bhargav, Prog. Org. Coat., 2020, 140, 105512.
44. Y. Shen, J. Tao, H. Tao, S. Chen, L. Pan and T. Wang, ACS Appl. Mater. Interfaces, 2015, 7, 20972-20978.
45. R. Nishimura, K. Hyodo, H. Mayama, S. Yokojima, S. Nakamura and K. Uchida,

Commun. Chem., 2019, 2, 90.

46. R. D. Podolsky, Science, 1994, 265, 100-103.

47. S. Chang, H. Qi, S. Zhou and Y. Yang, Appl. Therm. Eng., 2023, 219, 119516.